MATERIALS SCIENCE

Dynamic and programmable self-assembly of micro-rafts at the air-water interface

Wendong Wang,[1] Joshua Giltinan,[1,2] Svetlana Zakharchenko,[1]* Metin Sitti[1,2]†

Dynamic self-assembled material systems constantly consume energy to maintain their spatiotemporal structures and functions. Programmable self-assembly translates information from individual parts to the collective whole. Combining dynamic and programmable self-assembly in a single platform opens up the possibilities to investigate both types of self-assembly simultaneously and to explore their synergy. This task is challenging because of the difficulty in finding suitable interactions that are both dissipative and programmable. We present a dynamic and programmable self-assembling material system consisting of spinning at the air-water interface circular magnetic micro-rafts of radius 50 µm and with cosinusoidal edge-height profiles. The cosinusoidal edge-height profiles not only create a net dissipative capillary repulsion that is sustained by continuous torque input but also enable directional assembly of micro-rafts. We uncover the layered arrangement of micro-rafts in the patterns formed by dynamic self-assembly and offer mechanistic insights through a physical model and geometric analysis. Furthermore, we demonstrate programmable self-assembly and show that a 4-fold rotational symmetry encoded in individual micro-rafts translates into 90° bending angles and square-based tiling in the assembled structures of micro-rafts. We anticipate that our dynamic and programmable material system will serve as a model system for studying nonequilibrium dynamics and statistical mechanics in the future.

INTRODUCTION

Dynamic self-assembled material systems operate far from equilibrium and need constant energy input (1). Examples include supramolecular assemblies (2), various active colloids (3, 4), millimeter spinning discs (5, 6), and ferrofluid droplets (7). These works are driven mostly by two main quests. The first is to extend the existing equilibrium thermodynamics and statistical mechanics to nonequilibrium systems and to provide a theoretical framework to understand the dynamics of living systems, such as swarms and the origin of life (8–10). The second quest is to extend decades of works on static (equilibrium) self-assembly (11, 12) to obtain complex material architecture and to seek previously unseen or unexpected emergent properties and functions (13, 14).

Programmable self-assembly entails that information encoded in the parts are passed onto the whole (15). It is the implicit rationale behind the bottom-up synthesis in supramolecular chemistry (16) and nanochemistry (17), where chemical information embedded at the molecular and colloidal levels manifests itself in the final assembled structures through the works of molecular and intermolecular forces. Typical examples include mesoporous materials (18, 19), block copolymers (20), colloidal crystals (21), and, most quintessentially, DNA-based assemblies, such as DNA origami (22, 23) and DNA-attached colloidal particles (24–26). In an analogy to chemical bonds, the concept of capillary bonds (27, 28), proposed nearly two decades ago and based on patterning wettability of centimeter-scale objects floating at fluidic interfaces, was shown to provide some programmability.

Conceptually, the combination of dynamic and programmable self-assembly was demonstrated at millimeter scale by robotic swarms. However, their onboard batteries, sensors, and processors are difficult to be miniaturized to submillimeter scale (29). Encoding and programming with purely physical interactions at micrometer scales re-

main a great challenge, and solving this challenge is immensely beneficial for fields such as medicine (30, 31).

Here, we use recent experimental and theoretical advances on near-field capillary repulsion between micrometer-scale objects with sinusoidal edge-height profiles (32) and build a dynamic system by balancing the attractive interactions owing to a confining magnetic potential and the capillary repulsions owing to cosinusoidal edge-height profiles. Although similar to the previous system of millimeter-scale flat spinning discs in the use of an overall magnetic potential to provide attractive interactions (5), the use of near-field repulsive capillary interaction is the distinguishing feature of our system. Specifically, the air-water interface around a micro-raft is deformed by the curved height profile of the micro-raft's edge and contained both upward and downward menisci. Like menisci attract, whereas unlike menisci repel (33, 34). When spun at high-enough speed, micro-rafts are constantly reoriented such that the average interaction is repulsive and that micro-rafts are kept apart. When the spinning speed is lowered, the time for like menisci to align and attract each other increases. Below a certain threshold of spinning speed, the tendency for micro-rafts to align themselves overtakes the tendency for the external magnetic torque to misalign them, and the micro-rafts assemble. The repulsive hydrodynamic force, which was shown to be proportional to the disc radius to the power seven (6), is of minor importance in our system because we lowered the magnitude of the repulsive hydrodynamic interactions below that of the capillary interactions by setting the micro-rafts' radii to be 50 µm (figs. S1 to S3).

RESULTS

Parametric design of micro-rafts

Figure 1 illustrates the parametric modeling and characterization of a representative three-dimensional–printed (3D printed) micro-raft. Three main features of this micro-raft are the number n (= 4) of cosinusoidal curve profiles around the edge, the arc angle θ (= 30°) of each profile, and their amplitude A (= 4 µm) (Fig. 1A). Each of them can be changed parametrically. Because 6-fold symmetry is the most stable
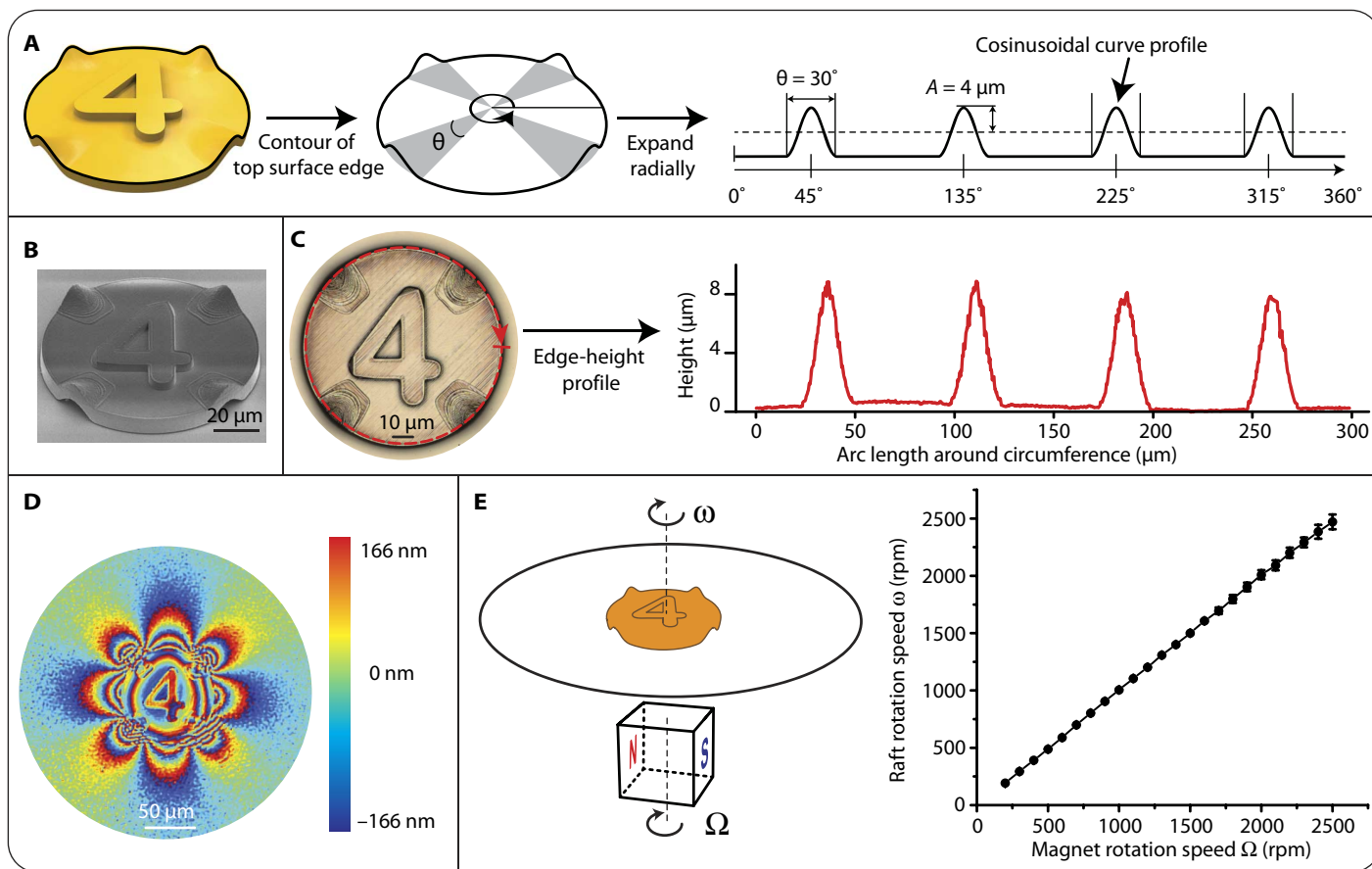
Fig. 1. The parametric design and characterization of one representative 3D printed micro-raft. (**A**) The essential features of the micro-raft include the number n (= 4) of cosinusoidal curve profiles around the edge, the arc angle θ (= 30°) of each profile's span, and the amplitude A (= 4 μm) of each profile. (**B**) SEM image of a representative micro-raft. (**C**) An overlap of a laser confocal image and an optical image on the left, and the extracted edge-height profile on the right, demonstrating the fidelity of fabrication. (**D**) The phase image extracted from a digital holograph of the micro-raft floating at the air-water interface, showing the interfacial deformation caused by the micro-raft. (**E**) The schematic of the magnetic torque generation on a micro-raft at the air-water interface using a rotating permanent magnet and the linear relationship between the magnet rotation speed Ω and the micro-raft rotation speed ω.

packing geometry of circular rafts [see, for example, bubble rafts by Bragg and Nye (35)], we chose $n = 4$ to test whether we can enforce 4-fold symmetry in the programmable self-assembly (more details later). The relief "4" on the top surface not only provides identification but also enables tracking micro-raft orientation and rotation in the video processing afterward. We varied arc angle θ and amplitude A in our experiments.

The high fidelity of the 3D microfabrication is demonstrated through the scanning electron microscope (SEM) image and the height profile extracted from a 3D laser confocal image (Fig. 1, B and C). Printing one micro-raft takes about 1 min, so the fabrication process can be scaled up to hundreds of micro-rafts within hours. Placed on the water surface, the micro-raft deforms the air-water interface, and this deformation is imaged with a digital holographical microscope, producing an interference pattern that reflects the micro-raft's 4-fold symmetry (Fig. 1D). A layer of cobalt is sputtered on the micro-raft to render it magnetic, and another layer of gold is added to prevent the oxidation of cobalt and to enable further functionalization of the micro-raft surface through a self-assembled monolayer (SAM). We use a rotating permanent magnet as energy input for our dynamic system (see fig. S4 for the experimental setup), and the rotation speed of the micro-raft ω is linear with respect to that of the magnet Ω (Fig. 1E).

Studies of pairwise interactions

Inspired by the method used in studying animal swarms (36), we started investigating our dynamic self-assembly system by studying pairwise interactions (Fig. 2). While spinning around their individual central axes at an angular speed ω (linear with respect to the spin speed of the permanent magnet Ω), the two micro-rafts are kept apart at a distance d from each other by capillary repulsion and are orbiting around a common center with an angular precession speed ω_p, where subscript p denotes precession (Fig. 2A). We analyzed videos of two micro-rafts spinning as a function of Ω and extracted the distance d and the precession speed ω_p from each video (see movie S1 for an example). Three typical sets of results are shown in Fig. 2 (B to D). In all sets, micro-rafts with zero amplitude attached to each other as soon as being introduced inside the attractive magnetic potential because they did not generate repulsive capillary interactions. In addition, we observed the following trends: (i) Higher amplitudes induce assembling at higher Ω's; (ii) thicker cobalt film increases the magnetic force that draws the micro-raft toward the center and pushes the onset of assembling to higher Ω's; and (iii) surface hydrophobization pushes the onset of the assembling to lower Ω's.

We also noted two interesting details. First, for micro-rafts with $A = 2$ to 4 μm, the angular precession speed ω_p increases with decreasing Ω
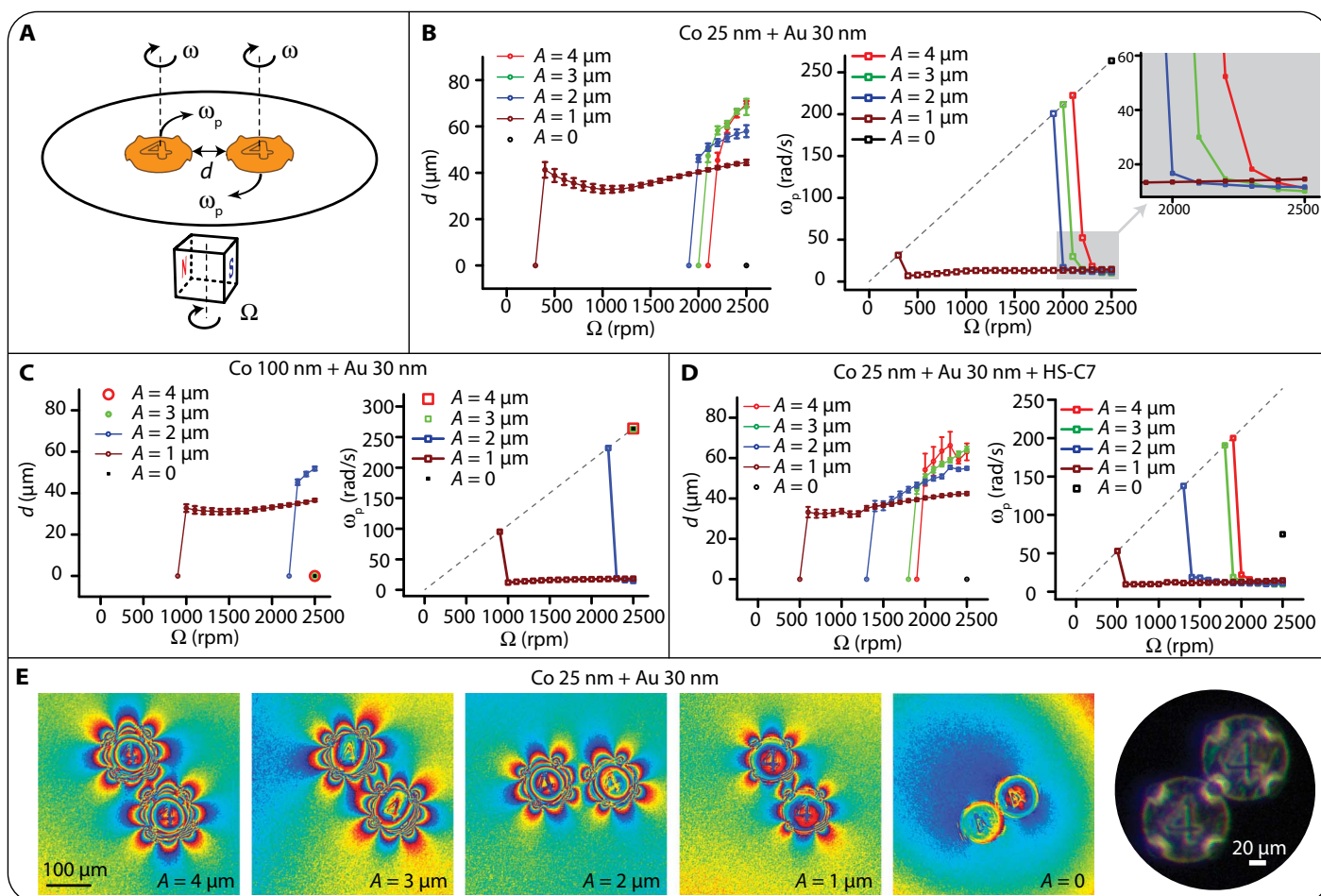
Fig. 2. Studies of pairwise interactions between two micro-rafts. (**A**) Schematic showing magnet rotation speed Ω, individual micro-raft rotation speed ω, edge-to-edge distance d, and precession speed ω_p. (**B**) Plots of d and ω_p versus Ω for micro-rafts coated with 25-nm cobalt and 30-nm gold. Higher amplitudes create larger separations and induce capillary assembly ($d = 0$) at higher critical Ω's. The dashed line in the ω_p versus Ω plot corresponds to the line $\omega_p = \Omega$. The zoomed-in region shows an increase in ω_p for $A = 2$ to 4 μm before assembling, suggesting capillary coupling near the onset of assembling. The control micro-rafts with $A = 0$ assemble at 2500 rpm, because no capillary repulsion exists between them. (**C**) Plots of d and ω_p versus Ω for micro-rafts coated with 100-nm cobalt and 30-nm gold. The overall magnetic potential created by the permanent magnet exerts stronger attractive interactions for micro-rafts with 100-nm cobalt than for micro-rafts with 25-nm cobalt. Therefore, the onsets of assembling shift to higher Ω's for all A's. (**D**) Plots of d and ω_p versus Ω for micro-rafts coated with 25-nm cobalt and 30-nm gold and further functionalized by a layer of SAM of heptanethiol (HS-C7) to make the micro-raft surface hydrophobic. The general trend of surface hydrophobization is to push the onset of assembling toward lower Ω's. (**E**) The first five images are the phase images obtained from a digital holographic microscope (DHM) for two micro-rafts of various amplitudes. All images were taken when the micro-rafts were spinning at 2500 rpm. The rightmost image is an optical microscope image showing a typical assembled structure. The arc angle θ is 30° for all micro-rafts in this figure.

before the onset of assembling, which suggests capillary coupling between two micro-rafts before assembling. Micro-rafts with $A = 1$ μm do not have this capillary coupling, probably because of smaller air-water interface deformation (Fig. 2E) and weaker capillary interactions. Second, micro-rafts with $A = 0$ and hydrophobic surfaces can rotate around their individual central axes even though their edge-to-edge distance d appears to be zero from the microscope image. We observed this phenomenon not only in micro-rafts coated with hydrophobic thiols but also in micro-rafts that had been stored in air for a few days and, hence, hydrophobized by the dust particles adsorbed on the gold surface (table S1). Taken as a whole, studying pairwise interactions provides us with a strategy to evaluate and compare different micro-rafts and to assess the microfabrication process. It is therefore an essential first step for all subsequent studies on dynamic and programmable self-assembly microsystems (fig. S5).

In an effort to gain further insight, we proceed with a simple dimensional analysis. We assume that the deformation of the water-air interface caused by one cosinusoidal edge-height profile scales with the amplitude of the profile A (1 to 4 μm) and its arc length $R\theta$ (~50 μm × $\pi/6$). The resulting capillary force should scale with $\gamma AR\theta/d$ (~10^{-8} to 10^{-7} N), with d being the distance between two micro-rafts. This capillary force is attractive if two cosinusoidal edges from two micro-rafts face each other and repulsive if they do not. In addition, if two cosinusoidal edges are not perfectly aligned, a capillary torque exists to rotate them back to alignment and should scale with $\gamma AR\theta^2(R + d/2)/4d$ (~10^{-12} to 10^{-11} N·m). When aligned, the two micro-rafts are drawn closer toward each other, whereas when misaligned, they are pushed away from each other. As a result, the separation distance between micro-rafts oscillates around an average value as long as the magnetic torque $\mathbf{m} \times \mathbf{B}$ can overcome the capillary torque and keep the micro-rafts rotating. If, at a particular moment,

the magnetic torque becomes smaller than the capillary torque, then the two micro-rafts assemble.

In addition, we include preliminary equilibrium simulations of capillary forces and torques using the Surface Evolver program in fig. S6 and outline the complexity of various competing interactions in the ensuing notes. We built upon these simulations a simple pairwise model that captures the assembling transition in fig. S7. Simulations that also include nonequilibrium aspects of the system, such as magnetic torque input and finite velocity of the capillary wave, are ongoing work in our laboratory. Although the crude and simple scaling analysis cannot explain all the features in pairwise interactions, it provides an adequate model for analyzing the patterns in dynamic self-assembly in the next section.

Dynamic self-assembly

Next, we study patterns of dynamic self-assembly of 3 to 40 micro-rafts. (To avoid confusion, we reserve the words "assemble" and "assembly" to denote situations in which micro-rafts attach to each other as in the studies of pairwise interactions and later in programmable self-assembly, and we use the word "pattern" to denote spatiotemporal arrangement of micro-rafts in dynamic self-assembly hereafter.) In any given pattern, the micro-rafts orbit around a common center at a constant precession speed. The trajectories of micro-rafts form approximately circular bands and thus provide the basis for organizing micro-rafts into layers (Fig. 3A). Counting the number of micro-rafts in each layer serves as a convenient way to label each pattern and enables us to identify polymorphs (an example is shown in Fig. 3B and movie S2). To further understand these dynamic patterns and validate the assumption that the main balance in our system is between the attractive overall magnetic potential and the repulsive capillary force, we modified the previous model (6) by replacing the repulsive hydrodynamic term with repulsive capillary terms

$$\frac{d\boldsymbol{r}_i}{dt} = \sum_{j \neq i} \frac{R^3 \boldsymbol{\omega} \times (\boldsymbol{r}_i - \boldsymbol{r}_j)}{|\boldsymbol{r}_i - \boldsymbol{r}_j|^3} \\ + (6\pi\mu R)^{-1} \left(c_m m \frac{d^2 B_x}{dx^2} \boldsymbol{r}_i + c_c \gamma A R \theta \sum_{j \neq i} \frac{(\boldsymbol{r}_i - \boldsymbol{r}_j)}{|\boldsymbol{r}_i - \boldsymbol{r}_j|} \frac{1}{|\boldsymbol{r}_i - \boldsymbol{r}_j| - 2R} \right), \\ i = 1, \dots N$$

where $\boldsymbol{r}_i$ is the position of the center of micro-raft i, $|\boldsymbol{r}_i - \boldsymbol{r}_j|$ is the center-to-center distance, and $|\boldsymbol{r}_i - \boldsymbol{r}_j| - 2R$ is the edge-to-edge distance. The first term on the right-hand side accounts for velocity field of the water generated by the rotation of the micro-rafts: R is the radius of the micro-raft, and ω is its angular velocity. The second term on the right-hand side accounts for the overall magnetic potential: μ is the dynamic viscosity of water; c_m is a constant of proportionality; m is the magnetic moment of one micro-raft; and $d^2 B_x/dx^2$ is the slope in B_x versus x plot for a 5-mm cubic magnet at $z = 6$ mm (fig. S3B). The slope is negative, which indicates that the overall potential draws the micro-rafts toward the center. The last term is the capillary term, where we adopted the scaling analysis in the previous section on pairwise interaction. c_c is a constant of proportionality; γ is the surface tension of water; A is the amplitude of a cosinusoidal profile; and θ is the arc angle of the profile. The capillary interaction on micro-raft i by micro-raft j is directed from j to i, and it is repulsive. The dynamic patterns are simulated by numerical integration of the equations above (refer to the "Simulation" section of the Supplementary Materials for more details).

The model can reproduce all 40 experimental dynamic patterns. It also produces many polymorphs. Many of these polymorphs have not been observed experimentally and may be due to the approximations made in the model. Patterns made of up to 19 micro-rafts are similar to the patterns reported in the millimeter-scale system (6). This resemblance prompted us to look for a simpler explanation for the dynamic patterns. By constructing Voronoi cells for all micro-rafts, we notice that the numbers of nearest neighbors for micro-rafts in inner layers is always close to 6 (Fig. 3C and movie S3; see fig. S8 for the complete list of 3 to 40 micro-rafts). Given that the most stable configuration in two dimensions is hexagonal packing, we think that the micro-rafts are "close-packed" by the overall magnetic potential in both dynamic systems and form a quasi-hexagonal structure.

The model also enables us to perform statistical tests on the relative rate of occurrence for each polymorph of a certain number of micro-rafts. For example, of 100 simulations for 21 micro-rafts, 75 of them are (2, 7, 12), and 25 of them are (1, 7, 13). As comparisons, of 100 simulations for 20 micro-rafts, 99 are (1, 7, 12), and only 1 is (2, 7, 11); by contrast, of 100 simulations for 22 micro-rafts, 45 of them are (2, 7, 13), 54 of them are (2, 8, 12), and only 1 is (1, 7, 14). These relative rates of occurrence for polymorphs of 20 to 22 micro-rafts seem to suggest a transition from one micro-raft at the center to two micro-rafts at the center. Experimental observation agrees with this statistical trend (Fig. 3A). Furthermore, in the spirit of the research on magic number in atomic clusters (37–39), a close inspection of Fig. 3A suggests that the maximum numbers of micro-rafts in the first and second layers are 5 and 10, respectively. These observations demand explanations that may be beyond what models based on equilibrium mechanics can offer (concepts such as energy minimization and metastable states may not apply here because the system is driven out of equilibrium), and they are interesting topics for nonequilibrium modeling in the future.

Programmable self-assembly

We employ the consistent relative positions of micro-rafts in the patterns of dynamic self-assembly as reliable initial conditions for studying assembling behavior of micro-rafts. We first show the assembling behaviors of three and four micro-rafts (Fig. 4). Three free micro-rafts consistently formed a structure with a bending angle of 90°, whereas two assembled micro-rafts and one free micro-raft consistently formed a linear structure (Fig. 4, A and B). A close look at the assembling processes (movie S4) shows that the assembly of three free micro-rafts started with the assembly of two micro-rafts, and the final micro-raft was attached to its nearest available cosinusoidally curved edge (henceforth called docking site), which, owing to their relative positions in the dynamic structure, was at 90° with respect to the already attached micro-raft. By contrast, in the case of two assembled micro-rafts and one free micro-raft (movie S5), the free micro-raft was orbiting around the assembled two micro-rafts and could only access the docking sites that were at the ends of the assembled structure, so the final assembled structure was linear. Similarly, four micro-rafts formed a right angle if all were free, and they formed a line if three of them were already assembled in a line (Fig. 4, C and D, and movies S6 and S7). The comparison of these two sets of experiments demonstrated the dependence of assembled structures on the initial conditions; the uses of different initial conditions in creating different structures are hitherto rarely, if at all, used in self-assembly.

Contrary to micro-rafts with arc angles of 30°, micro-rafts with arc angles of 90° assembled less deterministically and showed a variety of assembling behaviors (Fig. 4E). Four cosinusoidal curves of 90° arc
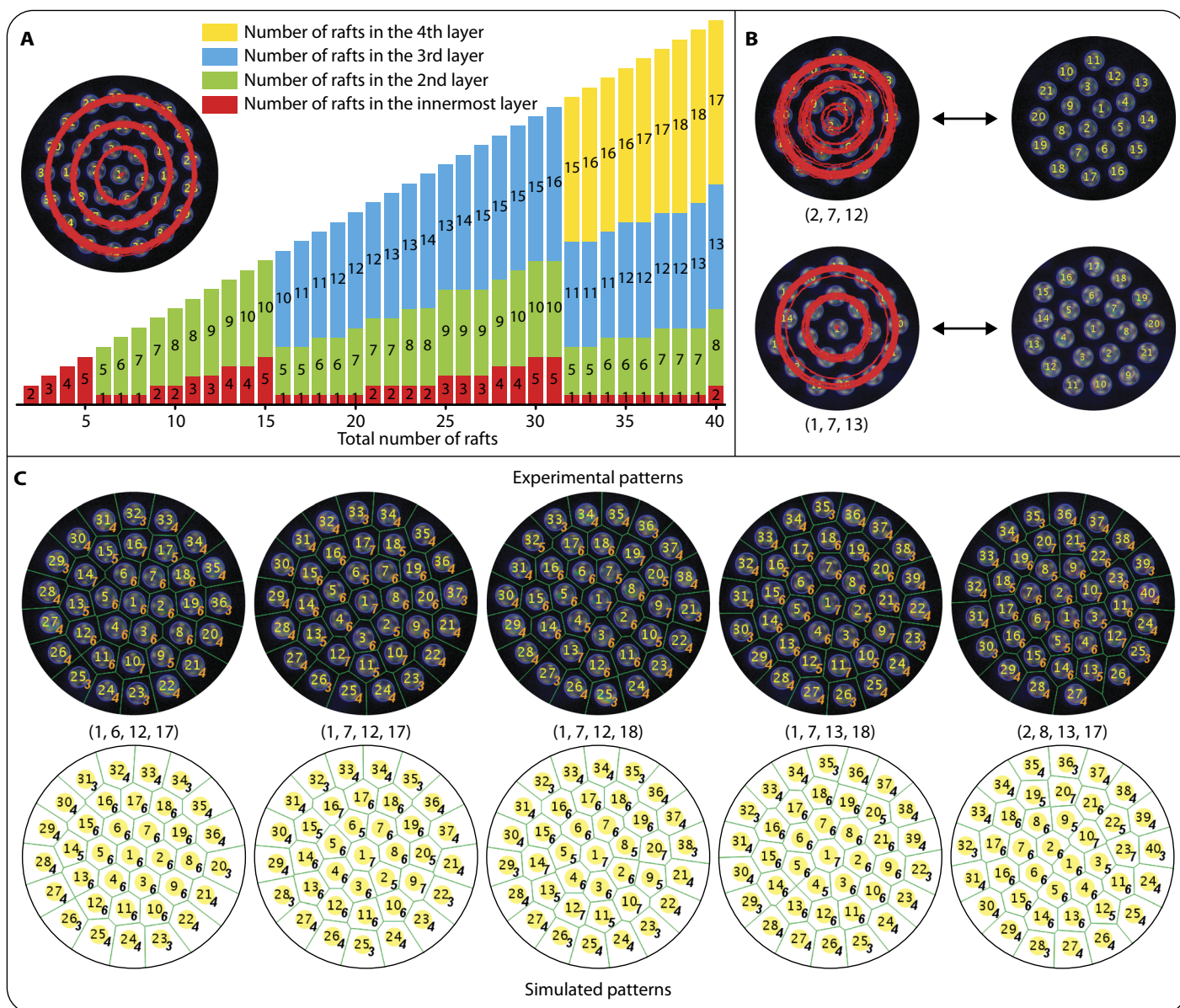
Fig. 3. Dynamically self-assembled patterns formed by up to 40 micro-rafts. (**A**) Numbers of micro-rafts in each layer for up to 40 micro-rafts. The inset on the top left shows four distinct bands formed by the trajectories of 36 micro-rafts. The central band consists of the trajectory of only one micro-raft. (**B**) An example of experimentally observed polymorphism is the two polymorphs of 21 micro-rafts. The top row shows two micro-rafts in the innermost layer, whereas the bottom row shows only one micro-raft in the innermost layer. The number at the center of a raft is the raft number, and the numbering starts from the innermost layer and increases clockwise within one layer. (**C**) Experimental and simulated patterns for 36 to 40 micro-rafts. The number in italics at the bottom right of each raft indicates the number of its nearest neighbors. This analysis of nearest neighbors is based on Voronoi cell construction, and it shows that the micro-rafts in the inner layers contain 6 ± 1 neighbors.

angle around a circular edge connect the cosine curves with each other at their troughs, and both peaks and troughs become potential docking sites (fig. S9). Consequently, the assembled structure may contain bending angles of both 90° and 45°, as illustrated in the four assembled structures (movie S8). The connectivity of the curve profiles around the edge also makes it less energetically costly for micro-rafts to roll around each other's edge and enables the assembled structure to reconfigure when the spinning speed is increased. Most configurations were not stable at high spinning speeds, which resulted in their eventual disassembly (movie S9), but two were stable: a diamond shape and a square shape (movies S10 and S11). The diamond shape

resembles the double triangular configurations predicted by Plateau's laws for stable aggregates of four bubbles (40), in which the only stable junctions are three bubbles meeting at angles of 120° (fig. S10). Unique in our system is the stable square shape, which reflects the 4-fold symmetry imbedded in individual micro-rafts.

Finally, we show the assembly of 40 micro-rafts (Fig. 5 and movies S12 to S14). Micro-rafts with arc angles of 30° assemble into mostly square-based patterns. Observed defects include triangle-based or pentagon-based shapes. In contrast, micro-rafts with arc angles of 90° assemble into mostly random shapes. This randomness is probably due to the low-energy barrier for micro-rafts to roll around each other
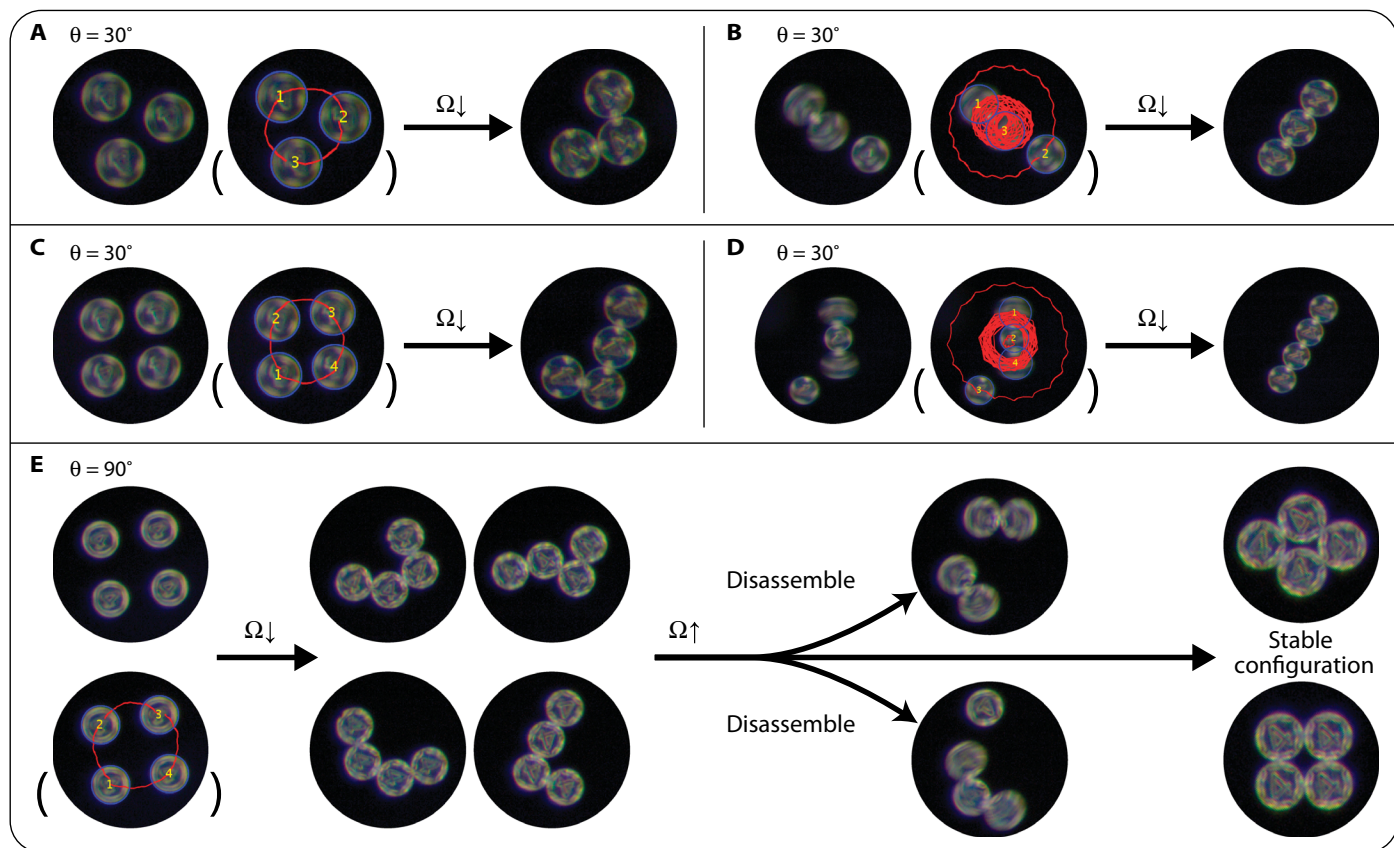
Fig. 4. Assembly of three to four micro-rafts through change of spinning speeds and the translation of symmetry from individual micro-rafts to assembled structures. (**A** to **D**) Deterministic assembly of three to four micro-rafts with arc angle θ = 30°: (A) From the initial triangular positions in the dynamic self-assembly state, three micro-rafts formed a right angle in the assembled structure. (B) From the initial conditions of two assembled micro-rafts and one free micro-raft, three micro-rafts formed a line. (C and D) Similar right-angled structure and linear structure form for four micro-rafts, from an initial four free micro-rafts and one free micro-raft, respectively. (**E**) Nondeterministic assembly of four micro-rafts with arc angle θ = 90°. The assembled structures show both 90° and 45° bending angles. When the spinning speed was again increased, the structures could disassemble or reconfigure into either a diamond or a square configuration. The amplitude A is 1 μm for all the micro-rafts in this figure.

and the increased number of docking sites. By repeatedly increasing and decreasing the rotation speed of the permanent magnet Ω, we obtained highly ordered, square-based tiling of micro-rafts with an arc angle of 30° at intermediate Ω (1000 to 1500 rpm). This process resembles the "annealing" process in crystal growth, where crystallinity increases by repeated heating and cooling. However, some disruption of this order at low Ω (500 to 200 rpm) reintroduces defects of triangular or pentagonal shapes.

DISCUSSION
Our results have shown that introducing cosinusoidal height profiles around the edge of micro-rafts not only generates near-field repulsive capillary interactions necessary for dynamic self-assembly, but also embeds directionality in individual micro-rafts, which manifests itself in programmable self-assembly.

Moreover, we demonstrated a process for studying a dynamic and programmable material system, namely, the process of investigating one, two, a few, and many components. This methodology will aid future exploration of micro-rafts of other sizes and shapes. We also highlighted the importance of pairwise interaction as the first step in probing dynamics and programmability of a system. Indeed, experimentally, the

information on separation distance and the onset of assembly, both obtained from pairwise interactions, is critical for identifying batch-to-batch differences during fabrication steps and for fine-tuning initial conditions used in programmable self-assembly.

Although our simple model based on scaling analysis is capable of producing patterns of dynamic self-assembly, it is unable to explain all the features observed in the pairwise interaction. More detailed modeling and simulation are ongoing research efforts in our laboratory to elucidate the mechanism underlying those features.

Moving forward, the flexibility afforded in our design and fabrication processes enables us to easily vary the size and the shape of the micro-rafts and to explore many conceptually interesting questions generic to all self-assembly systems, such as defects, chirality, hierarchy, phase separation, and density-dependent emergent properties (*41*). Our long-term vision is to provide a model system for nonequilibrium mechanics that will hold relevance in broader scientific and technological areas. In addition, the insights gained in this research would be beneficial to the design and development of reconfigurable microsystems (*42, 43*), mechanical gears at fluidic interfaces (*44*), reconfigurable optical components at submillimeter scale (*45*), and self-assembling microrobotic swarms for potential in vivo biomedical applications (*31*).
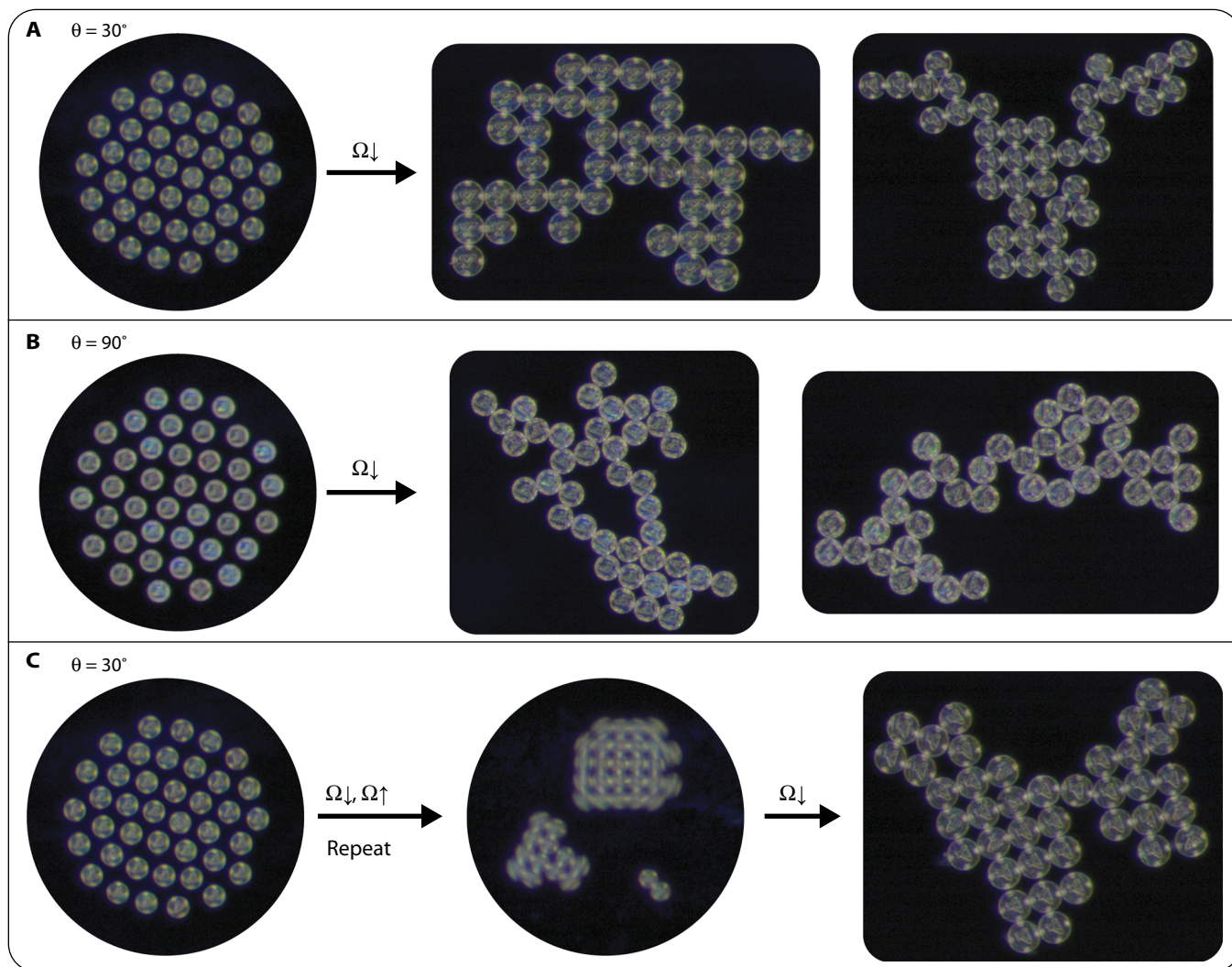
Fig. 5. Assembly of 40 micro-rafts. Assembly of 40 micro-rafts with arc angles of (**A**) 30° and (**B**) 90°. Note the difference between the mostly square-based tiling in (A) and random aggregates in (B). (**C**) Repeatedly decreasing and increasing the rotation speed of the permanent magnet Ω results in highly ordered, square-based tiling of micro-rafts at intermediate Ω (1000 to 1500 rpm). Some disruption of this order at low Ω (500 to 200 rpm) results in imperfections in the assembly, such as triangular or pentagonal shapes. The amplitude A is 1 μm for all the micro-rafts in this figure.

MATERIALS AND METHODS
Design, fabrication, and characterization of micro-rafts
Micro-rafts were designed in Rhinoceros 3D with the algorithmic modeling plug-in Grasshopper. Models of micro-rafts were then 3D-printed on Nanoscribe Photonic Professional GT with 63× oil immersion lens. The slicing and hatching distances were 0.3 and 0.2 μm, respectively. Thin films of cobalt and gold were sputtered using Kurt J. Lesker NANO 36. Cobalt was sputtered at 100 W and under a sputtering vacuum of ~4.0×10^{-3} mbar; gold was sputtered at 40 W and under a sputtering vacuum of ~2.8×10^{-3} mbar. SEM images of the micro-rafts were taken on the EO Scan Vega XL at 5 kV. Laser scanning confocal microscope images were taken on the Keyence VK-X200 series. SQUID measurement was performed on the Quantum Design MPMS XL with the range ±1 T.

Preparation of SAM
1-Heptanethiol was purchased from Sigma-Aldrich (H4506) and used without purification. Ethanol absolute (99.5%; 397691000, extradry AcroSeal, Acros Organics) was used as the solvent. Samples were immersed in 3 to 5 mM 1-heptanethiol solution for 2 to 24 hours under argon, after which they were rinsed five times in pure ethanol.

Experimental setup
A 5-mm cube NdFeB magnet (N42) was placed on a plastic petri dish filled with a layer of parafilm oil as lubricant. The magnetic field of the magnet was measured with the Lake Shore Model 460 3-Channel Gaussmeter and a three-axis probe. A digital stir plate (IKA Big Squid White) was used to spin the permanent magnet. A two-piece custom-made sample holder was used to provide an open air-water interface of ~30 mm in diameter as the working area. The top part of the sample holder was 3D printed on the Stratasys Objet 260 Connex3; the material was VeroClear RGD810. The bottom part was made from two plates of Plexiglas, cut by the Epilog Mini 24 Laser. The four rubber feet were printed with the TangoBlackPlus FLX980. Before each experiment, 2.50 ml of distilled and filtered (200 nm) water was filled in the sample holder to maintain consistent distance between the magnet and the top

of the air-water interface. Micro-rafts were lifted from the glass coverslip substrate by an oil painting brush (da Vinci red sable #0) and carefully placed on the air-water interface.

Video recording and analysis of the dynamics of spinning micro-rafts

Videos were recorded at 300 fps using the Basler acA800-510uc camera mounted on a stereomicroscope (Zeiss Discovery V12). They were analyzed using a custom script in MATLAB. DHM images were recorded and analyzed on Lyncée Tec reflection DHM R2200. DHM is also used to measure the distance between the top of the magnet and the air-water interface. The error bars of every point in the distance plots of pairwise interactions were estimated from 300 video frames for each point.

Simulations

Simulation of the magnetic field was performed on COMSOL Multiphysics 5.2 with an AC/DC module. Simulations of the dynamic patterns were performed on MATLAB 2016a. Please refer to the Supplementary Materials for details. Capillary energy simulations were performed on the Surface Evolver 2.7.

SUPPLEMENTARY MATERIALS

Supplementary material for this article is available at http://advances.sciencemag.org/cgi/content/full/3/5/e1602522/DC1

table S1. Contact angles of noncoated and SAM-coated gold surface.

fig. S1. Scaling analysis of various forces in the system.

fig. S2. In-plane magnetization of cobalt thin films.

fig. S3. Magnetic profile of a 5-mm cube magnet.

fig. S4. Photos of the experimental setup.

fig. S5. Pairwise interaction plots for micro-rafts used in Figs. 3 to 5.

fig. S6. Preliminary quantitative studies of micro-raft pairwise interactions using the Surface Evolver program.

fig. S7. Simulated pairwise interaction curves.

fig. S8. Experimental and simulated dynamic patterns for 3 to 40 micro-rafts.

fig. S9. Comparison between the digital holographical micrographs of micro-rafts with arc angles of 30° and 90°.

fig. S10. Unstable and stable configurations of aggregates of four bubbles.

movie S1. Examples of pairwise interactions.

movie S2. Two polymorphs of the dynamic patterns formed by 21 micro-rafts.

movie S3. Four examples of nearest-neighbor counts in dynamically self-assembled patterns.

movie S4. The assembly of three free micro-rafts with an arc angle of 30°.

movie S5. The assembly of one free and two attached micro-rafts with an arc angle of 30°.

movie S6. The assembly of four free micro-rafts with an arc angle of 30°.

movie S7. The assembly of one free and three attached micro-rafts with an arc angle of 30°.

movie S8. The assembly of four free micro-rafts with an arc angle of 90°.

movie S9. The disassembly of four assembled micro-rafts with an arc angle of 90°.

movie S10. The rearrangement of four assembled micro-rafts with an arc angle of 90° into a diamond shape.

movie S11. The rearrangement of four assembled micro-rafts with an arc angle of 90° into a square shape.

movie S12. The assembly of 40 micro-rafts with an arc angle of 30°.

movie S13. The assembly of 40 micro-rafts with an arc angle of 90°.

movie S14. The local rearrangement of assembled structures of 40 micro-rafts with an arc angle of 30° at intermediate spinning speed.

REFERENCES AND NOTES

1. G. M. Whitesides, B. Grzybowski, Self-assembly at all scales. *Science* **295**, 2418–2421 (2002).
2. E. Mattia, S. Otto, Supramolecular systems chemistry. *Nat. Nanotechnol.* **10**, 111–119 (2015).
3. W. Wang, W. Duan, S. Ahmed, A. Sen, T. E. Mallouk, From one to many: Dynamic assembly and collective behavior of self-propelled colloidal motors. *Acc. Chem. Res.* **48**, 1938–1946 (2015).
4. A. Snezhko, Complex collective dynamics of active torque-driven colloids at interfaces. *Curr. Opin. Colloid Interface Sci.* **21**, 65–75 (2016).
5. B. A. Grzybowski, H. A. Stone, G. M. Whitesides, Dynamic self-assembly of magnetized, millimetre-sized objects rotating at a liquid-air interface. *Nature* **405**, 1033–1036 (2000).
6. B. A. Grzybowski, H. A. Stone, G. M. Whitesides, Dynamics of self assembly of magnetized disks rotating at the liquid–air interface. *Proc. Natl. Acad. Sci. U.S.A.* **99**, 4147–4151 (2002).
7. J. V. I. Timonen, M. Latikka, L. Leibler, R. H. A. Ras, O. Ikkala, Switchable static and dynamic self-assembly of magnetic droplets on superhydrophobic surfaces. *Science* **341**, 253–257 (2013).
8. M. C. Marchetti, J. F. Joanny, S. Ramaswamy, T. B. Liverpool, J. Prost, M. Rao, R. Aditi Simha, Hydrodynamics of soft active matter. *Rev. Mod. Phys.* **85**, 1143–1189 (2013).
9. S. Ramaswamy, The mechanics and statistics of active matter. *Annu. Rev. Condens. Matter Phys.* **1**, 323–345 (2010).
10. S. Mann, Self-assembly and transformation of hybrid nano-objects and nanostructures under equilibrium and non-equilibrium conditions. *Nat. Mater.* **8**, 781–792 (2009).
11. G. M. Whitesides, J. P. Mathias, C. T. Seto, Molecular self-assembly and nanochemistry: A chemical strategy for the synthesis of nanostructures. *Science* **254**, 1312–1319 (1991).
12. G. A. Ozin, Nanochemistry: Synthesis in diminishing dimensions. *Adv. Mater.* **4**, 612–649 (1992).
13. B. A. Grzybowski, W. T. S. Huck, The nanotechnology of life-inspired systems. *Nat. Nanotechnol.* **11**, 585–592 (2016).
14. W. L. Noorduin, A. Grinthal, L. Mahadevan, J. Aizenberg, Rationally designed complex, hierarchical microarchitectures. *Science* **340**, 832–837 (2013).
15. L. Cademartiri, K. J. M. Bishop, Programmable self-assembly. *Nat. Mater.* **14**, 2–9 (2015).
16. J.-M. Lehn, *Supramolecular Chemistry: Concepts and Perspectives* (VCH Verlagsgesellschaft mbH, 1995).
17. G. A. Ozin, A. Arsenault, L. Cademartiri, *Nanochemistry: A Chemical Approach to Nanomaterials* (Royal Society of Chemistry, ed. 2, 2008).
18. C. T. Kresge, M. E. Leonowicz, W. J. Roth, J. C. Vartuli, J. S. Beck, Ordered mesoporous molecular sieves synthesized by a liquid-crystal template mechanism. *Nature* **359**, 710–712 (1992).
19. F. Hoffmann, M. Cornelius, J. Morell, M. Fröba, Silica-based mesoporous organic–inorganic hybrid materials. *Angew. Chem. Int. Ed.* **45**, 3216–3251 (2006).
20. J. Y. Cheng, C. A. Ross, H. I. Smith, E. L. Thomas, Templated self-assembly of block copolymers: Top-down helps bottom-up. *Adv. Mater.* **18**, 2505–2521 (2006).
21. Y. Yin, A. P. Alivisatos, Colloidal nanocrystal synthesis and the organic–inorganic interface. *Nature* **437**, 664–670 (2005).
22. Y. Ke, L. L. Ong, W. M. Shih, P. Yin, Three-dimensional structures self-assembled from DNA bricks. *Science* **338**, 1177–1183 (2012).
23. N. C. Seeman, DNA in a material world. *Nature* **421**, 427–431 (2003).
24. W. B. Rogers, V. N. Manoharan, Programming colloidal phase transitions with DNA strand displacement. *Science* **347**, 639–642 (2015).
25. C. A. Mirkin, R. L. Letsinger, R. C. Mucic, J. J. Storhoff, A DNA-based method for rationally assembling nanoparticles into macroscopic materials. *Nature* **382**, 607–609 (1996).
26. A. P. Alivisatos, K. P. Johnsson, X. Peng, T. E. Wilson, C. J. Loweth, M. P. Bruchez Jr., P. G. Schultz, Organization of 'nanocrystal molecules' using DNA. *Nature* **382**, 609–611 (1996).
27. N. Bowden, A. Terfort, J. Carbeck, G. M. Whitesides, Self-assembly of mesoscale objects into ordered two-dimensional arrays. *Science* **276**, 233–235 (1997).
28. N. Bowden, I. S. Choi, B. A. Grzybowski, G. M. Whitesides, Mesoscale self-assembly of hexagonal plates using lateral capillary forces: Synthesis using the "capillary bond". *J. Am. Chem. Soc.* **121**, 5373–5391 (1999).
29. M. Rubenstein, A. Cornejo, R. Nagpal, Programmable self-assembly in a thousand-robot swarm. *Science* **345**, 795–799 (2014).
30. M. Sitti, Miniature devices: Voyage of the microrobots. *Nature* **458**, 1121–1122 (2009).
31. M. Sitti, H. Ceylan, W. Hu, J. Giltinan, M. Turan, S. Yim, E. Diller, Biomedical applications of untethered mobile milli/microrobots. *Proc. IEEE* **103**, 205–224 (2015).
32. L. Yao, L. Botto, M. Cavallaro Jr., B. J. Bleier, V. Garbin, K. J. Stebe, Near field capillary repulsion. *Soft Matter* **9**, 779–786 (2013).
33. L. Botto, E. P. Lewandowski, M. Cavallaro Jr., K. J. Stebe, Capillary interactions between anisotropic particles. *Soft Matter* **8**, 9957–9971 (2012).
34. D. Vella, L. Mahadevan, The "cheerios effect". *Am. J. Phys.* **73**, 817–825 (2005).
35. L. Bragg, J. F. Nye, A dynamical model of a crystal structure. *Proc. R. Soc. Lond. A Math. Phys. Sci.* **190**, 474–481 (1947).
36. J. Gautrais, F. Ginelli, R. Fournier, S. Blanco, M. Soria, H. Chaté, G. Theraulaz, Deciphering interactions in moving animal groups. *PLOS Comput. Biol.* **8**, e1002678 (2012).
37. O. Echt, K. Sattler, E. Recknagel, Magic numbers for sphere packings: Experimental verification in free xenon clusters. *Phys. Rev. Lett.* **47**, 1121–1124 (1981).
38. H. W. Kroto, The stability of the fullerenes C_n, with n = 24, 28, 32, 36, 50, 60 and 70. *Nature* **329**, 529–531 (1987).
39. M. K. Harbola, Magic numbers for metallic clusters and the principle of maximum hardness. *Proc. Natl. Acad. Sci. U.S.A.* **89**, 1036–1039 (1992).

40. D. A. W. Thompson, *On Growth and Form* (Cambridge Univ. Press, ed. 2, 1942).

41. Y. Goto, H. Tanaka, Purely hydrodynamic ordering of rotating disks at a finite reynolds number. *Nat. Commun.* **6**, 5994 (2015).

42. G. Z. Lum, Z. Ye, X. Dong, H. Marvi, O. Erin, W. Hu, M. Sitti, Shape-programmable magnetic soft matter. *Proc. Natl. Acad. Sci. U.S.A.* **113**, E6007–E6015 (2016).

43. S. Miyashita, E. Diller, M. Sitti, Two-dimensional magnetic micro-module reconfigurations based on inter-modular interactions. *Int. J. Robot. Res.* **32**, 591–613 (2013).

44. J. M. K. Ng, M. J. Fuerstman, B. A. Grzybowski, H. A. Stone, G. M. Whitesides, Self-assembly of gears at a fluid/air interface. *J. Am. Chem. Soc.* **125**, 7948–7958 (2003).

45. S. K. Y. Tang, R. Derda, A. D. Mazzeo, G. M. Whitesides, Reconfigurable self-assembly of mesoscale optical components at a liquid-liquid interface. *Adv. Mater.* **23**, 2413–2418 (2011).

Citation: W. Wang, J. Giltinan, S. Zakharchenko, M. Sitti, Dynamic and programmable self-assembly of micro-rafts at the air-water interface. *Sci. Adv.* **3**, e1602522 (2017).

The following resources related to this article are available online at
http://advances.sciencemag.org. (This information is current as of May 25, 2017):

Updated information and services, including high-resolution figures, can be found in the online version of this article at:
http://advances.sciencemag.org/content/3/5/e1602522.full

Supporting Online Material can be found at:
http://advances.sciencemag.org/content/suppl/2017/05/22/3.5.e1602522.DC1

This article **cites 42 articles,** 11 of which you can access for free at:
http://advances.sciencemag.org/content/3/5/e1602522#BIBL